Title

Strong Potential Gradients and Electron Confinement in ZnO Nanoparticle Films: Implications for Charge-Carrier Transport and Photocatalysis

Journal

ACS Applied Nano Materials, 4(11)

ISSN

2574-0970

Authors

Mahl, Johannes

Gessner, Oliver

Barth, Johannes V

et al.

Publication Date

2021-11-26

DOI

10.1021/acsanm.1c02730

Peer reviewed

Strong Potential Gradients and Electron Confinement in Nanostructured ZnO

Johannes Mahl[1], Oliver Gessner[1], Johannes V. Barth[2], Peter Feulner[2] and Stefan Neppl[1,3]*

[1]Chemical Sciences Division, Lawrence Berkeley National Laboratory, 94720 Berkeley, USA

[2]Physikdepartment E20, Technische Universität München, 85747 Garching, Germany

[3]Paul Scherrer Institut, 5232 Villigen, Switzerland

* corresponding author: stefan.neppl@psi.ch

Abstract:

Zinc oxide (ZnO) nanomaterials are promising components for chemical and biological sensors, and operate as electron collectors in photovoltaic technologies. Many of these applications involve nanostructures in contact with liquids or exposed to ambient atmosphere. Under these conditions, single crystal ZnO surfaces are known to form narrow electron accumulation layers with few-nm spatial penetration into the bulk. A key question is to what extent such pronounced surface potential gradients can develop in the nanophases of ZnO, where they are expected to dominate the catalytic activity by modulating charge carrier mobility and lifetimes. Here, we follow the temperature-dependent surface electronic structure of nanoporous ZnO with photoemission spectroscopy to reveal a sizable, spatially averaged downward band bending for the hydroxylated state, and a conservative upper bound of <6 nm for the spatial extent of the associated potential gradient, which implies strong confinement of the conduction-band electrons to the surface of the nanostructure.

Keywords:

nanostructures, zinc oxide, band bending, electron confinement, photoemission spectroscopy, surface metallization

Introduction:

Nanoscale zinc oxide (ZnO) attracts broad interest in fundamental research and for industrial applications, as it can be economically and sustainably synthesized in a vast variety of shapes, ranging from spherical particles, pillars, discs and ribbons, to more complex and extended architectures like tetrapods or cauliflowers.[1] This design flexibility is the main reason for its success in nano-electronics, chemical/biological sensors, photocatalytic remediation, as well as energy conversion and storage schemes.[1–3] The crystalline phase, orientation, and aspect ratio in these nanostructures can further be tailored to meet specific application demands, facilitating rational device optimization.[4]

However, aside from these prospects, ZnO materials also exhibit a complex defect chemistry, which often complicates the prediction and microscopic interpretation of their function in electronic and catalytic applications .[1] For example, it is still controversial what types of impurities are responsible for its native n-type conductivity, and what role these defect states play in mediating chemical reactions.[5–7] Most defects are formed preferentially near the surface, and are therefore believed to dominate the electronic and catalytic response of metal-oxide nanomaterials. The electronic structure of ZnO interfaces is therefore governed by intrinsic and adsorbate-induced donor/acceptor states, which can disturb the local charge balance near the

surface, giving rise to the formation of space charge layers (SCLs). The depth-dependent potential $V_{bb}(z)$ associated with this charge imbalance modifies all energy levels in the near-surface region of the semiconductor, commonly referred to as "band bending" (bb) effect.[8] Depending on the characteristics of this band bending, the resultant potential energy landscape can either be a driving force for efficient electron-hole pair separation, or for the localization of one charge carrier type near the surface, which are both critical gateways for boosting (photo-)chemical reaction yields.[8] In particular, the weaker photocatalytic performance of rutile TiO_2 single crystals compared to the anatase phase has been explained by the smaller surface band bending present at rutile surfaces.[9] Although band bending is beneficial for many applications, it is usually considered to be negligibly small in nanomaterials.[8,9] Here we demonstrate that under hydroxylated conditions sizeable band bending can develop in nanostructured ZnO, which strongly impacts its interfacial electronic structure.

Many applications of ZnO nanostructures require the material to be in contact with liquids or involve exposure to ambient humidity. Extensive research on single crystal ZnO has demonstrated that these conditions lead to a hydroxylation of the ZnO surfaces. The associated surface hydroxyl groups are mainly formed between ZnO surface oxygen atoms and intermediate protons generated, e.g., during the dissociative adsorption of water, alcohols, or hydrogen.[10–19] They induce shallow donor states that easily release electrons into the ZnO conduction band (CB).[20–23] This adsorbate-mediated surface transfer doping generates positively charged donors at the surface, and accumulates negative charge within the SCL. The underling interfacial charge rearrangement leads to a downward bending of all energy levels near the surface, and may even

trigger semiconductor-to-metal phase transitions when the CB minimum (CBM) is shifted below the Fermi level.[10,24,25]

Despite enormous research efforts, however, it remains unclear to what extent nano-sized ZnO structures are able to accommodate significant interfacial potential gradients.[8,26,27] For ZnO nanomaterials exposed to different gases, or subject to different surface treatments, indications for both upward and downward *bb* have been reported, suggesting that the *bb* character results from the interplay between adsorbate-adsorbate and surface-adsorbate interactions.[14,28–33] Detailed, quantitative information on the polarity, magnitude, and shape of $V_{bb}(z)$ under well-controlled conditions is therefore necessary to obtain a comprehensive understanding of the catalytic function of ZnO nanostructures on a microscopic level. Unfortunately, common spectroscopic techniques established for the characterization of extended, single-crystal semiconductors lack sensitivity to the shape of $V_{bb}(z)$ as a function of the depth z below the surface, or yield ambiguous results when applied to nanoporous or amorphous samples.[8]

Here, we follow the temperature-controlled evolution of the near-surface electronic structure of ZnO nanoparticle films (~15 nm average particle diameter) with X-ray (XPS) and ultraviolet (UPS) photoemission spectroscopy under UHV conditions (see Supporting Information (SI) for details). Our results provide conclusive evidence for a significant, ~0.8 eV spatially averaged downward *bb* for the initially hydroxylated surface, with a <6 nm maximum spatial penetration of the associated potential gradient into the bulk of the nanoparticle film. These findings are crucial for understanding and optimizing charge carrier transport in interconnected metal-oxide nanoparticle networks and their (photo-)catalytic performance.

Results and Discussion:

Figure 1(a) compares O1s XPS spectra acquired from the hydroxylated ZnO nanostructure, as loaded at room temperature (top panel), as well as after annealing to T_S = 400 K (middle panel) and to T_S = 700 K (bottom panel). The presence of surface OH-groups is verified by the high binding energy O1s component at E_B = 532.7 eV (green).[12,13] The total O1s photoemission is described by a pair of Gaussian peaks with fixed E_B separation (1.6 eV) and constrained full-width-at-half-maximum (FWHM). Assuming a flat substrate, and taking the 2.3 Å average thickness of hydroxyl monolayers on low-index ZnO surfaces as a reference,[13,34] the 38% hydroxyl contribution to the total O1s emission (in combination with the 1.57 nm inelastic mean free path (IMFP) of the O1s photoelectrons[35]) translates into an OH-coverage of ~3 monolayers. Including the impact of the corrugated nanostructure surface on the relative O1s XPS signal strengths within a single-sphere approximation leads to a ~50% smaller estimate for the OH-coverage (see Supporting Information (SI)).[36] Thus, as the real surface topography of the fused ZnO nanoparticle films lies in between these limiting scenarios, the measured O1s peak intensity ratio is fully consistent with a complete hydration of the ZnO samples at room temperature. Upon annealing to T_S = 700 K, the OH-related O1s peak decreases below the detection limit, indicating the transition to a surface hydroxyl-free ZnO nanostructure. This threshold temperature range for complete OH removal is in good agreement with XPS results from both polar and non-polar ZnO crystal surfaces,[12,13] temperature-dependent conductivity measurements,[37] and thermal desorption studies on ZnO powders.[38]

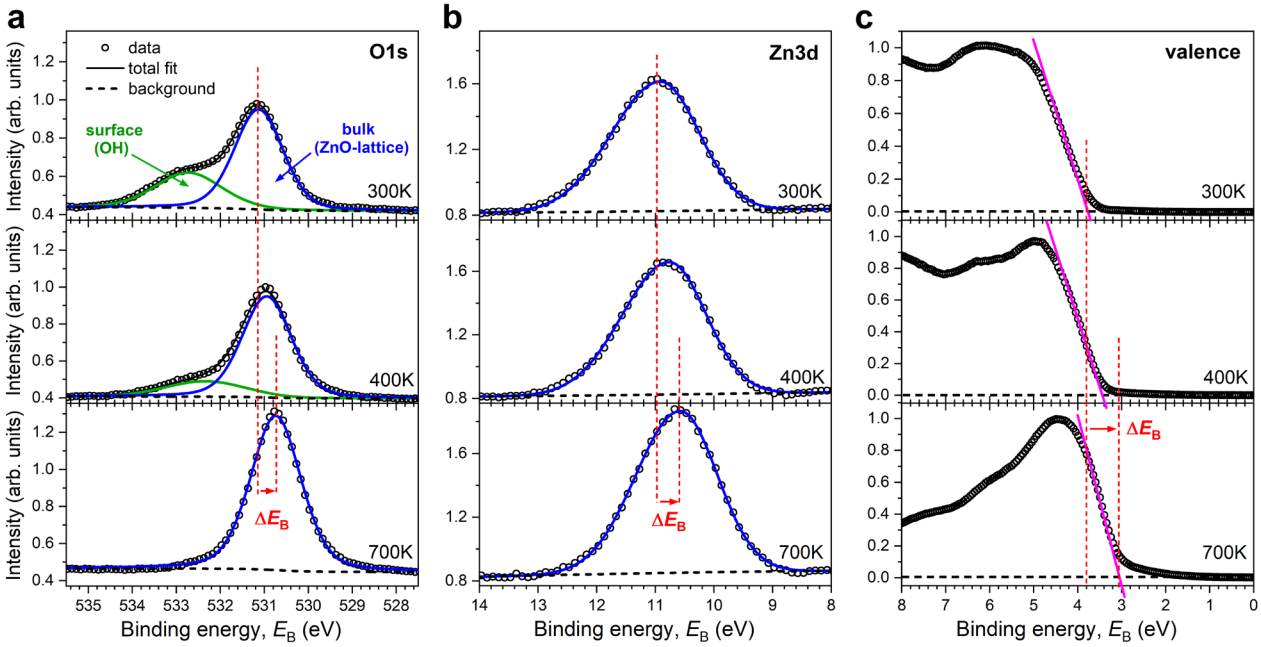

Figure 1. Temperature-dependent XPS and UPS spectra of a ZnO nanoparticle film. (a) O1s XPS spectra obtained for the initially hydroxylated sample at 300 K (top), and after annealing to 400 K (middle) and 700 K (bottom) in UHV. The O1s photoemission is decomposed into a ZnO-bulk (blue solid lines) and surface hydroxyl (OH) contribution (green solid lines). (b) Zn3d XPS spectra. (c) UPS valence band spectra. The position of the valence band maximum (VBM) at the surface is determined by linear extrapolation of the low binding energy edge (magenta solid lines) to the baseline. UPS and XPS spectra are recorded with photon energies of $h\nu$ = 21.2 eV and $h\nu$ = 1253.6 eV, respectively. Red dashed lines highlight the temperature-induced shifts to lower binding energies (ΔE_B-O1s: 470 meV; ΔE_B-Zn3d: 380 meV; ΔE_B-VBM: 790 meV).

As indicated by the red dashed lines in Figure 1(a,b), the loss of OH-groups is accompanied by rigid shifts of the O1s and Zn3d photoemission lines to lower E_B. The same trend is observed for the valence band maximum (VBM) as indicated by the UPS spectra in Figure 1(c). The intersection of a linear fit to the leading edge of the VB photoemission and the instrument baseline yields a binding energy of E_{VBM}^{surf} = 3.74 ±0.02 eV for the VBM at the surface of the hydroxylated nanostructure (uncertainties are standard errors of several independent measurements). Note that this binding energy is significantly larger than the bandgap E_g= 3.30±0.01 eV of the nanoporous ZnO film (Figure S1, SI). Generally, for a non-degenerated n-

type semiconductor, a scenario where E_{VBM}^{surf} exceeds the material bandgap is only compatible with a downward bending of the electronic bands near the surface (Figure S3, SI).[8] Thus, the combination of the large VBM binding energy relative to the Fermi level and the intrinsic n-type behavior of bulk ZnO[39] is an unambiguous signature for downward *bb* toward the surface of the nanostructure.[10–13] Annealing the sample shifts the VBM at the surface closer to the Fermi level, saturating at a minimum value of E_{VBM}^{surf} = 2.95 ±0.02 eV for $T_S \gtrsim 600$ K.

Figure 2 summarizes the temperature-dependent evolution of several key parameters characterizing the electronic structure of the nanoporous ZnO surface. Distinct trends are observed with decreasing OH coverage (a): both E_{VBM}^{surf} (b) and the Zn3d peak (d) shift gradually to lower E_B, which can be attributed to a reduction of downward *bb*. Additionally, the workfunction (c) increases as a function of T_S, which is expected for a diminishing positive charge at the surface associated with the quenching of OH-related donors upon desorption at elevated temperatures.[14] A similar correlation between OH coverage, workfunction and E_{VBM}^{surf} has been found for ZnO single crystals upon controlled exposure to hydrogen, water and methanol.[10–12,14] In particular, the workfunction of 3.85 eV determined here for the as-loaded nanoporous film is almost identical to the value reported for completely hydrogen-terminated low-index ZnO surfaces,[11,14] which further corroborates the assumption of a fully hydroxylated initial state of the nanostructures investigated here.

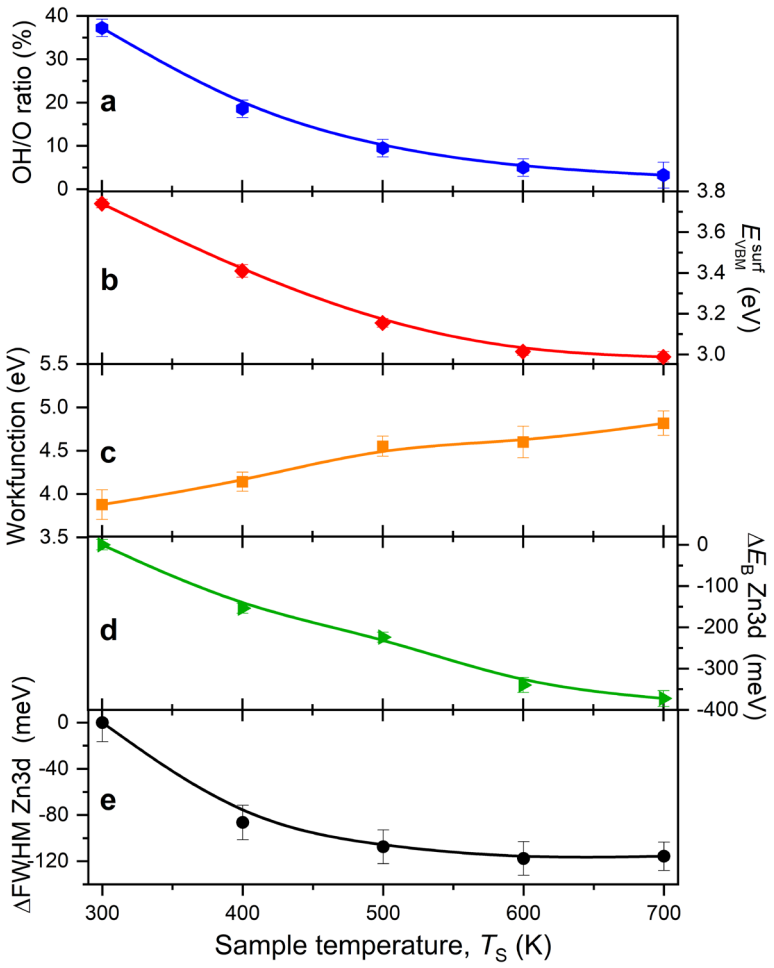

Figure 2. Temperature-dependent evolution of the surface electronic structure. (a) Contribution of the surface-hydroxyl component to the total O1s photoemission as function of sample temperature. (b) Position of the valence band maximum at the surface with respect to the Fermi level. (c) Workfunction derived from the low-energy cutoffs of the UPS spectra. (d) Binding energy of the Zn3d photoemission line. (e) Zn3d peak width (FWHM). Solid lines are guides to the eye.

Closer inspection of Figure 2(b,d,e) reveals that the Zn3d XPS peak experiences only roughly half the E_B -shift compared to the UPS-derived E_{VBM}^{surf}, which is accompanied by a distinct narrowing of its lineshape. The microscopic origin of these effects is illustrated in Figure 3(a-c): whenever the XPS probing depth is similar to the spatial extent of the SCL below the surface, the spectral distribution of the overall Zn3d photoemission is modulated by the interfacial potential gradient $V_{bb}(z)$. Therefore, starting from a downward *bb* scenario as illustrated in Figure 3(c),

temperature-driven band flattening (a,b) will be reflected in a narrowing of the Zn3d XPS peak width and a shift of its center toward lower binding energies, as experimentally observed. This combined effect of photoelectron escape depth and spatial $V_{bb}(z)$ progression on shaping the observed Zn3d signal is also responsible for the difference in energy shifts determined by UPS and XPS. In the more surface-sensitive UPS measurements of E_{VBM}^{surf}, photoelectrons originate almost exclusively from the topmost layer.[40] In contrast, the probing depth (defined as 3 x IMFP) in the Zn3d XPS experiments is ~3 x 2.35 nm,[35] which leads to significant averaging of photoelectron signals with different binding energies emerging from different depths, and thus to a smaller overall energy shift of the entire XPS spectrum as illustrated in Figure 3(a-b).

Based on the discussion presented so far, we interpret the saturation behavior of the temperature-dependent spectral signatures in Figure 2 as a transition from an initial downward *bb* situation in the as-loaded ZnO film, towards flatband conditions for the dehydrated state at $T_S \gtrsim 600$ K. In this context, the difference between E_{VBM}^{surf} at T_S = 300 K and T_S = 700 K directly yields the maximum downward *bb* at the surface V_{bb}^{surf} = 0.79 ±0.03 eV for the fully hydroxylated ZnO nanostructure, which allows us to determine the position of the conduction band minimum (CBM) in the bulk of the ZnO nanoparticles to be $E_{CBM}^{bulk} = V_{bb}^{surf} + E_g - E_{VBM}^{surf}$ = 350 meV above the Fermi level (see Figure S3, SI). Applying Boltzmann statistics and the effective mass approximation for the CB occupancy, we estimate the bulk carrier density of the nanoporous film to be $n_b = N_C \times e^{-E_{CBM}^{bulk}/k_BT} \approx 4 \cdot 10^{12}$ cm^{-3}, where $N_C \approx 3 \cdot 10^{18}$ cm^{-3} is the effective CB density of states in ZnO.[13] Such comparatively low values for n_b are in reasonable agreement with carrier densities expected for high-quality ZnO films,[41] and align with the core-shell structure proposed

for ZnO nanoparticles, i.e., a crystalline and stoichiometric bulk region surrounded by a highly defective surface.[31]

Temperature-driven *bb* modifications have recently been observed for various OH-terminated metal-oxide single-crystals.[12,13,42] In these systems, the transition from electron-accumulation-type SCLs to the flatband limit occurred in an intermediate temperature range, and was followed by the emergence of electron-depletion-type SCLs featuring upward *bb* at higher temperatures.[12,13,42] In general, it is difficult to unequivocally infer flatband conditions solely based on energy shifts in photoemission spectra.[43,44] In this context, the additional information revealed by the temperature-dependent Zn3d XPS peak width is essential. As indicated in Figure 3(a-c), the flatband situation is characterized by the narrowest XPS lineshape. In contrast, the onset of sizable upward *bb* at higher temperatures would inevitably add spectral broadening.[42,43] It is therefore important to note that not only the energy shifts, but also the FWHMs of the Zn3d peak for the last two annealing cycles are indistinguishable within the error margins (see Figure 2(d,e)). This favors flatband energy level alignment rather than electron depletion within the SCL during the final heat treatment employed in our study. Note that the UPS-determined VBM position also remains unchanged for T_S = 600-700 K within the experimental uncertainty (Figure 2(b)). This quantity tracks any change in the surface potential even more sensitively due to the small probing depth inherent to the UPS method.[40]

Since the correlation between the Zn3d peak shift and its line-narrowing encodes the spatial characteristics of the *bb* potential, we adopt an XPS peak envelope reconstruction algorithm to retrieve quantitative information on the $V_{bb}(z)$ depth profile from the T_S -dependent Zn3d E_B-

shifts and FWHM variations.[19,43,44] In this approach, the spectral distribution $D(E_B)$ of the total Zn3d emission is modeled as a superposition of discrete photoelectron contributions emerging from different depths z_i below the surface (Figure 3(a-c)) according to:

$$D(E_B) = \sum_i D_i = \sum_{i(\forall z, \in SCL)} D_0(E_B - E_0 - V_{bb}(z_i)) \times e^{-z_i/IMFP}.$$

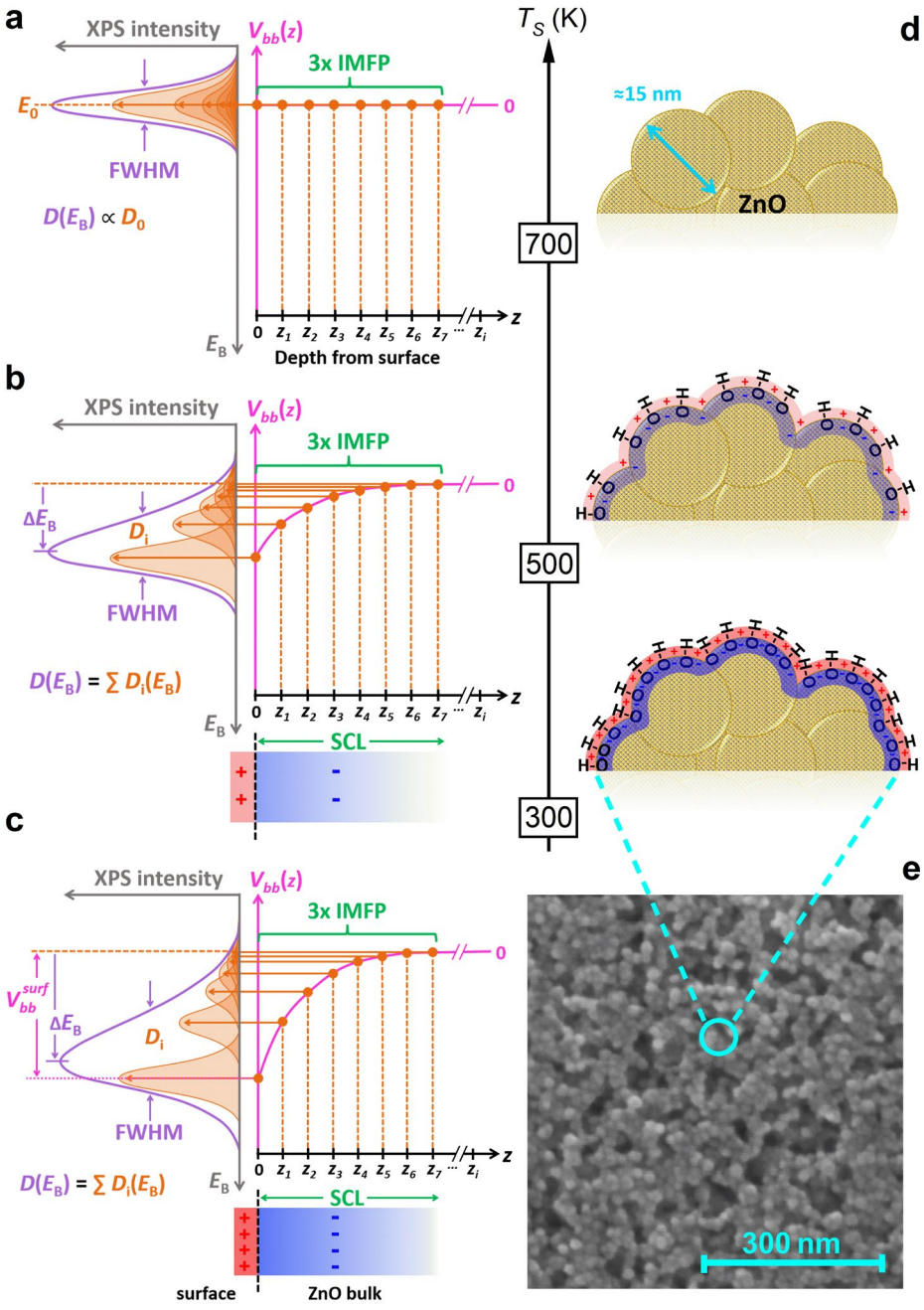

Figure 3. Correlation between Zn3d XPS lineshape, band bending and OH coverage. (a)-(c) The total Zn3d XPS spectrum $D(E_B)$ is modeled as a superposition of spectral contributions D_i emerging from different depths z_i below the interface. The relative D_i intensities are weighted by the inelastic mean free path (IMFP), and their central energies are governed by the local value of the band bending potential $V_{bb}(z_i)$. If the XPS probing depth (= 3 × IMFP) is comparable to the spatial extent of $V_{bb}(z)$, changes in this potential are mapped onto modulations of the overall XPS lineshape. Different scenarios are illustrated: (a) flatband condition resulting in the narrowest XPS lineshape. (b) Moderate, and (c) strong downward band bending giving rise to additional spectral broadening. (d) Schematics illustrating the correlation between the sample temperature T_S, surface hydroxylation and the space charge layer (SCL) that defines $V_{bb}(z)$. Note that the oxygen in the OH groups represents a ZnO surface atom. (e) SEM image of the ZnO nanoparticle film.[45]

Here, D_i and E_0 denote the Zn3d lineshape and peak position, respectively, in the absence of band bending, i.e., under flatband conditions ($V_{bb}(z) = 0$). For the simulations, we derive these input parameters from a Gaussian fit to the Zn3d spectrum at T_S = 700 K (Figure 1(b)). The relative spectral weights of the individual D_i components are defined by the exponential IMFP damping term. In all numerical calculations, the spatial sampling step size $z_{i+1} - z_i$ was set to 0.2 nm, which corresponds to the interlayer spacing of ZnO, averaged over all high-symmetry directions in the wurtzite lattice. By matching simulated to measured Zn3d XPS spectra, different analytic functions describing the $V_{bb}(z)$ shape can be benchmarked against the experimental ΔFWHM-vs.-ΔE_B trace, assuming that the depletion of surface donors only affects the magnitude of the downward band bending potential.

These simulations are illustrated in Figure 4(a), which shows fit results for a cubic potential profile, $V_{bb}(z) = V_{bb}^{surf} \times \left(\frac{z_{bb}-z}{z_{bb}}\right)^3$ for $0 \leq z \leq z_{bb}$, where V_{bb}^{surf} is the maximum band-bending value at the ZnO surface (z = 0) and z_{bb} is the maximum spatial extent of the band-bending potential into the bulk. Excellent agreement with the experimentally derived ΔFWHM-vs.-ΔE_B

trace (Figure 4(a)) and the Zn3d XPS spectra (Figure 4(b)) is achieved for z_{bb} = 5.1 ± 0.7 nm. Error bars represent the z_{bb}-range within which the merit function χ^2 is less than twice the minimum value, as shown in the inset of Figure 4(a). We tested several functional forms of $V_{bb}(z)$, the corresponding optimized depth profiles are summarized in Figure 4(c). A central finding is that the *bb* potential drops by more than 80% over a distance of less than 3 nm from the surface, irrespective of the exact $V_{bb}(z)$ model shape. While the existence of such strong interfacial potential gradients has been established for adsorbate-covered single-crystal ZnO surfaces,[10–14] our results strongly suggest that they can also develop in nanoscale structures.

It should be noted that the Zn3d XPS simulations presented here are based on a planar sample geometry. Corresponding simulations within a single-sphere model (SSM) yield an even smaller spatial extent of the built-in potential (see inset of Figure 4(d)) due to an effectively reduced IMFP (see SI). The interconnected nanoparticle films in our study can be assumed to exhibit surface topographies in between these two limiting cases.

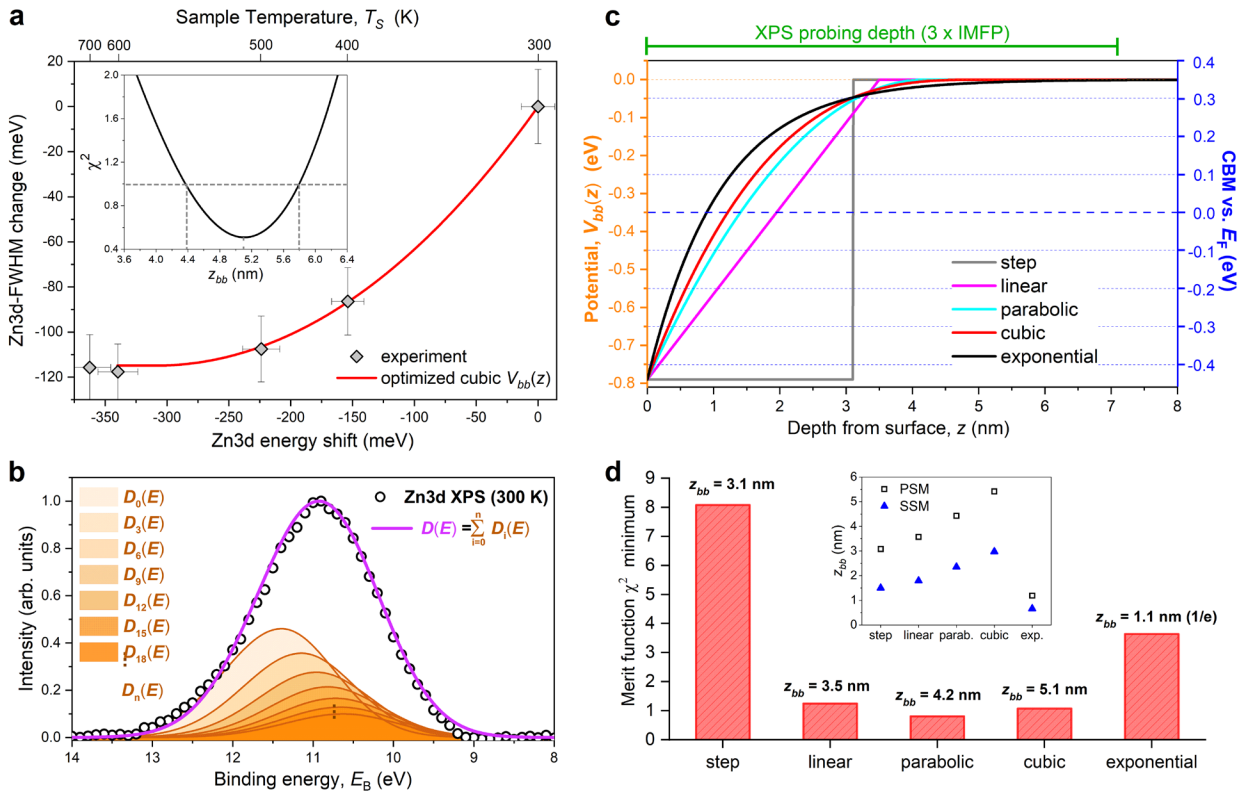

Figure 4. Quantifying the depth profile of the interfacial potential $V_{bb}(z)$. (a) Comparison of the experimentally determined correlation between Zn3d peak-shift and peak-narrowing to a numerical simulation based on a cubic $V_{bb}(z)$ profile. Parameter optimization restricts the maximum spatial extent of the potential to z_{bb} = 5.1 ± 0.7 nm below the surface. The nanometer sensitivity of this modeling is highlighted in the inset, showing the z_{bb}–dependence of the fit merit function. (b) Comparison of experimental (black circles) and simulated (violet solid line) Zn3d XPS spectrum at a sample temperature T_S = 300 K. The origins of the individual XPS components D_i (orange shaded peaks) are illustrated in Figure 3(a-c). (c) Comparison of analytical functions for $V_{bb}(z)$. The green bar indicates the experimental XPS probing depth of the Zn3d photoemission. The orange energy scale references the surface potential to the bulk limit, whereas the blue energy scale refers to the position of the conduction band minimum (CBM) vs. the Fermi level. (d) Merit function minima of simulations based on the $V_{bb}(z)$ shapes depicted in (c). Optimized z_{bb} parameters define the depths z where the potential reaches the ZnO bulk value. Only for the exponential profile is z_{bb} defined as the 1/e decay constant. The inset compares z_{bb} values obtained from an analysis within a planar-surface model (PSM) and a single-sphere model (SSM).

The determination of the most suitable analytical approximation for $V_{bb}(z)$ is illustrated in Figure 4(d). It compares the minima of the merit function for parameter-optimized simulations based on the different $V_{bb}(z)$ profiles depicted in Figure 4(c). Evidently, a step-like or exponential shape can be discarded, which further demonstrates the nanometer sensitivity of our approach to $V_{bb}(z)$ depth variations. Within the experimental uncertainties, it is difficult to distinguish between a linear, parabolic, and cubic $V_{bb}(z)$ shape based on the quality of the fit results alone. However, a linear potential profile is not linked to a well-defined carrier distribution $n_e(z)$ via the Poisson equation $\frac{d^2V_{bb}(z)}{dz^2} \propto n_e(z)$, and is therefore discarded. For a more detailed discussion of the parabolic and cubic potential shapes, it is instructive to consider general boundary conditions for potential gradients and underlying charge carrier densities in isolated ~15 nm ZnO nanoparticles. Solving the Poisson equation for spherical semiconductor particles,[27] we estimate that a uniform volume electron density of ~$7 \cdot 10^{19}$ cm^{-3} within the SCL shell is required for a parabolic $V_{bb}(z)$ to enable 0.8 eV downward *bb*. For comparison, a cubic $V_{bb}(z)$ can generate the same potential drop with a linear charge density increase from n_b = $4 \cdot 10^{12}$ cm^{-3} in the core region, to $6 \cdot 10^{19}$ cm^{-3} near the surface of the nanoparticles (see Figure S4, SI). Integrating the charge density profiles along the depth coordinate z yields $3 \cdot 10^{13}$ cm^{-2} and $1.5 \cdot 10^{13}$ cm^{-2} for the number of electrons per unit area associated with parabolic and cubic potential gradients, respectively. These values are consistent with carrier densities observed by Hall-measurements in electron accumulation layers of hydrogenated ZnO single crystals surfaces.[46]

To explore whether electron area densities of this magnitude can be generated solely by surface-hydroxyl donor states, we build on theoretical studies of water adsorption on ZnO($10\bar{1}0$),[16] which represents the lowest-energy ZnO surface, and is thus expected to be a prevalent crystal

orientation in ZnO nanomaterials. DFT calculations identify two H_2O molecules per ZnO($10\bar{1}0$) surface unit cell (0.33 x 0.52 nm^2) as the most stable monolayer configuration, with one H_2O moiety adsorbed molecularly, while the second dissociates. The intermediate hydrogen atom generated in the latter process combines with a surface lattice oxygen atom to form a surface OH-group with electron donor character.[16] This scenario yields an upper limit of ~$6 \cdot 10^{14}$ cm^{-2} for purely surface-hydroxyl-induced electron area densities, which is fully compatible with the interpretation of OH-mediated surface-transfer doping being the dominating source of electrons inside the SCL for the hydroxylated ZnO nanostructures.

Since most of the electrons in the ZnO SCL have been released from surface donor levels, the equilibrium electron density distribution is also expected to be graded towards the interface, shaped by Coulomb interaction and carrier diffusion processes. We therefore favor the cubic $V_{bb}(z)$ dependency as the simplest analytical description for the spatial depth evolution of the *bb* potential inside the ZnO nanoparticle film, albeit combinations of higher-degree polynomials might possibly yield slightly better agreement with the experiment. Interestingly, however, $V_{bb}(z)$ simulations based on single-term higher polynomial parameterizations consistently result in worse agreement with the experimental data compared to the cubic profile (Figure S5, SI). Future studies employing tunable X-ray photon energies may provide more stringent tests of such subtle microscopic details of the potential gradient.

Conclusion:

In summary, we provide strong evidence for large potential gradients within the surface-near region of hydroxylated ZnO nanostructures, with an average spatial extent of only a few nanometers into the bulk. Based on the corrugated nature of the nanostructure surface, the ~0.8

eV downward band bending revealed here should be considered as a spatially averaged property of the nanoporous film. Indeed, recent DFT studies on hydrogenated ZnO($10\bar{1}0$) surfaces emphasize the local character of such adsorbate-induced potentials, with atomic-scale spatial confinement to the adsorption sites and amplitude modulations exceeding 1 eV.[14] Contrary to common belief, our experiments indicate that band bending effects of this magnitude can also occur in metal-oxide nanomaterials, and has therefore to be considered in the description of their surface electronic properties. Recently, significant hydroxyl-related downward band bending has also been reported for single-crystal Ag/ZnO junctions.[19] The pronounced nanophase potential gradients revealed in the study reported here might therefore be of general importance for successfully interfacing metal contacts with ZnO nanostructures in device applications.

Finally, our results imply a partial metallization of the hydroxylated ZnO nanostructure surface, since the CBM near the interface is below the Fermi level (Figure 4(c)). The possibility to control and tailor such surface-conductive channels is relevant for advancing the performance of ZnO-based (photo-)catalytic nanomaterials. For example, near-surface diffusive transport of electrons through interconnected nanoparticle networks may activate surface-recombination pathways and lead to reduced device performance. We note that the findings presented here suggest a microscopic picture of electron propagation that is contrary to the most common models of charge transport in nanoporous metal-oxides. These usually assume depleted nanoparticles featuring upward band bending, where electron transfer proceeds via particle-to-particle hopping in a random-walk fashion. The surface electronic structure of hydroxylated nanoscale ZnO discovered here might be partly responsible for the comparably low performance of this material in dye-sensitized photo-electrochemical systems.[3,45]

Experimental Section:

Sample preparation: ZnO nanoparticles with an average diameter of ~15 nm have been prepared with a sol-gel method based on a zinc acetate dihydrate precursor (Sigma-Aldrich) in ethanoic solution and tetramethylammonium hydroxide as separating agent.[47] The resulting colloidal suspension is spin-coated (2000 rpm) onto cleaned 1 x 1 cm^2 mirror-like polished stainless steel or FTO substrates. The films are subsequently dried at 60 °C and calcinated in air at 360 °C for 50 minutes to generate interconnected nanoporous networks. This procedure yields macroscopically homogenous ZnO films, while preserving a nanoscale surface topography. The ~0.5 μm thick ZnO films were cleaned by ultra-sonication in ethanol and de-ionized water, and blown dry with Argon before transferring them into the UHV system (base pressure $<2 \cdot 10^{-10}$ mbar) for the XPS and UPS experiments. In the main text, these samples are referred to as initially hydroxylated ZnO nanoparticle films.

Photoemission experiments: UPS spectra are recorded using He-I emission ($h\nu$ = 21.2 eV) and XPS spectra with non-monochromatized MgKα radiation ($h\nu$ = 1253.6 eV) from a laboratory X-ray tube in normal photoelectron emission geometry. The absolute binding energy scale is calibrated with respect to the Fermi level at E_F = 0.00 eV and the $Au4f_{7/2}$ peak center at 84.00 eV, obtained from a sputter-cleaned gold surface. The resolution in the UPS and XPS experiments was ~150 meV and ~0.8 eV, respectively. In all measurements, the photon intensity was varied by at least one order of magnitude to exclude errors due to sample charging, especially for the dehydroxylated samples. Additional care was taken to rule out any impact of sample degradation upon prolonged He-I/X-ray exposure. Taking the sampling area of the hemispherical photoelectron energy analyzer into account (SPECS; Phoibos100 operated in medium-area

mode), we estimate that ~10^{10} individual nanoparticles contribute to the measured XPS and UPS signals reported here. For each annealing step, the sample was kept at a specific temperature for 5 min. Photoemission spectra were subsequently taken at a sample temperature of 300 K. The temperature was monitored with a type-K thermocouple pressed onto one corner of the sample. Sample annealing was performed by radiative heating from the rear with two tungsten filaments. Photoemission spectra obtained after annealing to >700 K are not discussed here, as such high-temperature treatments caused instabilities within the ZnO nanoparticle film, with partial loss of adhesion to the metal/FTO substrates.

Supporting Information:

Sample characterization, energy level schematics, charge density and band bending calculations for isolated nanoparticles, single-sphere model for XPS signal attenuation.

Conflict of Interest:

The authors declare no conflict of interest.

Acknowledgements:

This work was supported by the Atomic, Molecular, and Optical Sciences Program of the U.S. Department of Energy, Office of Science, Office of Basic Energy Sciences, Division of Chemical Sciences, Geosciences, and Biosciences at Lawrence Berkeley National Laboratory under Contract No. DE-AC02-05CH11231. J.M. acknowledges partial support from the Advanced Light Source Doctoral Fellowship. S.N. acknowledges financial support from the Alexander-Humboldt Foundation. J.V.B. and P.F. from the Deutsche Forschungsgemeinschaft (e-conversion

Cluster of Excellence). We thank Friedrich Esch from the Chemistry Department of the Technical University of Munich for extracting the ZnO nanoparticle size distribution from the SEM data.

References:

(1) Schmidt-Mende, L.; MacManus-Driscoll, J. L. ZnO – Nanostructures, Defects, and Devices. *Mater. Today* **2007**, *10* (5), 40–48. https://doi.org/10.1016/S1369-7021(07)70078-0.

(2) Özgür, Ü.; Hofstetter, D.; Morkoç, H. ZnO Devices and Applications: A Review of Current Status and Future Prospects. *Proc. IEEE* **2010**, *98* (7), 1255–1268. https://doi.org/10.1109/JPROC.2010.2044550.

(3) Zhang, Q.; Dandeneau, C. S.; Zhou, X.; Cao, G. ZnO Nanostructures for Dye-Sensitized Solar Cells. *Adv. Mater.* **2009**, *21* (41), 4087–4108. https://doi.org/10.1002/adma.200803827.

(4) Tian, Z. R.; Voigt, J. A.; Liu, J.; Mckenzie, B.; Mcdermott, M. J.; Rodriguez, M. A.; Konishi, H.; Xu, H. Complex and Oriented ZnO Nanostructures. *Nat. Mater.* **2003**, *2* (12), 821–826. https://doi.org/10.1038/nmat1014.

(5) Kim, Y.-S.; Park, C. H. Rich Variety of Defects in ZnO via an Attractive Interaction between O Vacancies and Zn Interstitials: Origin of n -Type Doping. *Phys. Rev. Lett.* **2009**, *102* (8), 086403. https://doi.org/10.1103/PhysRevLett.102.086403.

(6) Look, D. C.; Farlow, G. C.; Reunchan, P.; Limpijumnong, S.; Zhang, S. B.; Nordlund, K. Evidence for Native-Defect Donors in n -Type ZnO. *Phys. Rev. Lett.* **2005**, *95* (22), 225502. https://doi.org/10.1103/PhysRevLett.95.225502.

(7) Penfold, T. J.; Szlachetko, J.; Santomauro, F. G.; Britz, A.; Gawelda, W.; Doumy, G.; March, A. M.; Southworth, S. H.; Rittmann, J.; Abela, R.; Chergui, M.; Milne, C. J. Revealing Hole Trapping in Zinc Oxide Nanoparticles by Time-Resolved X-Ray Spectroscopy. *Nat. Commun.* **2018**, *9* (1), 478. https://doi.org/10.1038/s41467-018-02870-4.

(8) Zhang, Z.; Yates, J. T. Band Bending in Semiconductors: Chemical and Physical Consequences at Surfaces and Interfaces. *Chem. Rev.* **2012**, *112* (10), 5520–5551. https://doi.org/10.1021/cr3000626.

(9) Ozawa, K.; Emori, M.; Yamamoto, S.; Yukawa, R.; Yamamoto, S.; Hobara, R.; Fujikawa, K.; Sakama, H.; Matsuda, I. Electron−Hole Recombination Time at TiO2 Single-Crystal Surfaces: Influence of Surface Band Bending. *J. Phys. Chem. Lett.* **2014**, *5*, 1953.

(10) Ozawa, K.; Mase, K. Metallization of ZnO(10-10) by Adsorption of Hydrogen, Methanol, and Water: Angle-Resolved Photoelectron Spectroscopy. *Phys. Rev. B* **2010**, *81* (20), 205322. https://doi.org/10.1103/PhysRevB.81.205322.

(11) Ozawa, K.; Mase, K. Comparison of the Surface Electronic Structures of H-Adsorbed ZnO Surfaces: An Angle-Resolved Photoelectron Spectroscopy Study. *Phys. Rev. B* **2011**, *83* (12), 125406. https://doi.org/10.1103/PhysRevB.83.125406.

(12) Heinhold, R.; Williams, G. T.; Cooil, S. P.; Evans, D. A.; Allen, M. W. Influence of Polarity and Hydroxyl Termination on the Band Bending at ZnO Surfaces. *Phys. Rev. B* **2013**, *88* (23), 235315. https://doi.org/10.1103/PhysRevB.88.235315.

(13) Heinhold, R.; Cooil, S. P.; Evans, D. A.; Allen, M. W. Stability of the Surface Electron Accumulation Layers on the Nonpolar (10-10) and (11-20) Faces of ZnO. *J. Phys. Chem. C* **2014**, *118* (42), 24575–24582. https://doi.org/10.1021/jp507820m.

(14) Deinert, J.-C.; Hofmann, O. T.; Meyer, M.; Rinke, P.; Stähler, J. Local Aspects of Hydrogen-Induced Metallization of the ZnO (10-10) Surface. *Phys. Rev. B* **2015**, *91* (23), 235313. https://doi.org/10.1103/PhysRevB.91.235313.

(15) Dulub, O.; Meyer, B.; Diebold, U. Observation of the Dynamical Change in a Water Monolayer Adsorbed on a ZnO Surface. *Phys. Rev. Lett.* **2005**, *95* (13), 136101. https://doi.org/10.1103/PhysRevLett.95.136101.

(16) Meyer, B.; Marx, D.; Dulub, O.; Diebold, U.; Kunat, M.; Langenberg, D.; Wöll, C. Partial Dissociation of Water Leads to Stable Superstructures on the Surface of Zinc Oxide. *Angew. Chem. Int. Ed.* **2004**, *43* (48), 6641–6645. https://doi.org/10.1002/anie.200461696.

(17) Newberg, J. T.; Goodwin, C.; Arble, C.; Khalifa, Y.; Boscoboinik, J. A.; Rani, S. ZnO(10-10) Surface Hydroxylation under Ambient Water Vapor. *J. Phys. Chem. B* **2018**, *122* (2), 472–478. https://doi.org/10.1021/acs.jpcb.7b03335.
(18) Piper, L. F. J.; Preston, A. R. H.; Fedorov, A.; Cho, S. W.; DeMasi, A.; Smith, K. E. Direct Evidence of Metallicity at ZnO (000 1 ¯) − (1 × 1) Surfaces from Angle-Resolved Photoemission Spectroscopy. *Phys. Rev. B* **2010**, *81* (23), 233305. https://doi.org/10.1103/PhysRevB.81.233305.
(19) Chernysheva, E.; Srour, W.; Philippe, B.; Baris, B.; Chenot, S.; Duarte, R. F.; Gorgoi, M.; Cruguel, H.; Rensmo, H.; Montigaud, H.; Jupille, J.; Cabailh, G.; Grachev, S.; Lazzari, R. Band Alignment at Ag/ZnO(0001) Interfaces: A Combined Soft and Hard x-Ray Photoemission Study. *Phys. Rev. B* **2018**, *97* (23), 235430. https://doi.org/10.1103/PhysRevB.97.235430.
(20) Janotti, A.; Van de Walle, C. G. Hydrogen Multicentre Bonds. *Nat. Mater.* **2007**, *6* (1), 44–47. https://doi.org/10.1038/nmat1795.
(21) Van de Walle, C. G.; Neugebauer, J. Universal Alignment of Hydrogen Levels in Semiconductors, Insulators and Solutions. *Nature* **2003**, *423* (6940), 626–628. https://doi.org/10.1038/nature01665.
(22) Van de Walle, C. G. Hydrogen as a Cause of Doping in Zinc Oxide. *Phys. Rev. Lett.* **2000**, *85* (5), 1012–1015. https://doi.org/10.1103/PhysRevLett.85.1012.
(23) Cox, S. F. J.; Davis, E. A.; Cottrell, S. P.; King, P. J. C.; Lord, J. S.; Gil, J. M.; Alberto, H. V.; Vilão, R. C.; Piroto Duarte, J.; Ayres de Campos, N.; Weidinger, A.; Lichti, R. L.; Irvine, S. J. C. Experimental Confirmation of the Predicted Shallow Donor Hydrogen State in Zinc Oxide. *Phys. Rev. Lett.* **2001**, *86* (12), 2601–2604. https://doi.org/10.1103/PhysRevLett.86.2601.
(24) Wang, C.; Zhou, G.; Li, J.; Yan, B.; Duan, W. Hydrogen-Induced Metallization of Zinc Oxide (2-1-1 0) Surface and Nanowires: The Effect of Curvature. *Phys. Rev. B* **2008**, *77* (24), 245303. https://doi.org/10.1103/PhysRevB.77.245303.
(25) Wang, Y.; Meyer, B.; Yin, X.; Kunat, M.; Langenberg, D.; Traeger, F.; Birkner, A.; Wöll, Ch. Hydrogen Induced Metallicity on the ZnO (10-10) Surface. *Phys. Rev. Lett.* **2005**, *95* (26), 266104. https://doi.org/10.1103/PhysRevLett.95.266104.
(26) Albery, W. J.; Bartlett, P. N. The Transport and Kinetics of Photogenerated Carriers in Colloidal Semiconductor Electrode Particles. *J. Electrochem. Soc.* **1984**, *131* (2), 315–325. https://doi.org/10.1149/1.2115568.
(27) Goossens, A. Potential Distribution in Semiconductor Particles. *J. Electrochem. Soc.* **1996**, *143* (6), L131. https://doi.org/10.1149/1.1836900.
(28) Al-Saadi, M. J.; Al-Harthi, S. H.; Kyaw, H. H.; Myint, M. T. Z.; Bora, T.; Laxman, K.; Al-Hinai, A.; Dutta, J. Influence of Atomic Hydrogen, Band Bending, and Defects in the Top Few Nanometers of Hydrothermally Prepared Zinc Oxide Nanorods. *Nanoscale Res. Lett.* **2017**, *12* (1), 22. https://doi.org/10.1186/s11671-016-1800-3.
(29) Chen, C.-Y.; Retamal, J. R. D.; Wu, I.-W.; Lien, D.-H.; Chen, M.-W.; Ding, Y.; Chueh, Y.-L.; Wu, C.-I.; He, J.-H. Probing Surface Band Bending of Surface-Engineered Metal Oxide Nanowires. *ACS Nano* **2012**, *6* (11), 9366–9372. https://doi.org/10.1021/nn205097e.
(30) Eichel, R.-A.; Erdem, E.; Jakes, P.; Ozarowski, A.; Van Tol, J.; Hoffmann, R. C.; Schneider, J. J. Space-Charge Layer, Intrinsic "Bulk" and Surface Complex Defects in ZnO Nanoparticles — a High-Field Electron Paramagnetic Resonance Analysis. *Funct. Mater. Lett.* **2013**, *06* (04), 1330004. https://doi.org/10.1142/S1793604713300041.
(31) Kaftelen, H.; Ocakoglu, K.; Thomann, R.; Tu, S.; Weber, S.; Erdem, E. EPR and Photoluminescence Spectroscopy Studies on the Defect Structure of ZnO Nanocrystals. *Phys. Rev. B* **2012**, *86* (1), 014113. https://doi.org/10.1103/PhysRevB.86.014113.
(32) Merz, T. A.; Doutt, D. R.; Bolton, T.; Dong, Y.; Brillson, L. J. Nanostructure Growth-Induced Defect Formation and Band Bending at ZnO Surfaces. *Surf. Sci.* **2011**, *605* (9–10), L20–L23. https://doi.org/10.1016/j.susc.2010.12.021.
(33) Tay, Y. Y.; Tan, T. T.; Liang, M. H.; Boey, F.; Li, S. Specific Defects, Surface Band Bending and Characteristic Green Emissions of ZnO. *Phys. Chem. Chem. Phys.* **2010**, *12* (23), 6008. https://doi.org/10.1039/b926427b.
(34) Önsten, A.; Stoltz, D.; Palmgren, P.; Yu, S.; Claesson, T.; Göthelid, M.; Karlsson, U. O. SO2 Interaction with Zn(0001) and ZnO(0001) and the Influence of Water. *Surf. Sci.* **2013**, *608*, 31–43. https://doi.org/10.1016/j.susc.2012.09.007.

(35) Tanuma, S.; Powell, C. J.; Penn, D. R. Calculations of Electron Inelastic Mean Free Paths. V. Data for 14 Organic Compounds over the 50-2000 EV Range. *Surf. Interface Anal.* **1994**, *21* (3), 165–176. https://doi.org/10.1002/sia.740210302.
(36) Shard, A. G.; Wang, J.; Spencer, S. J. XPS Topofactors: Determining Overlayer Thickness on Particles and Fibres. *Surf. Interface Anal.* **2009**, *41* (7), 541–548. https://doi.org/10.1002/sia.3044.
(37) Göpel, W.; Lampe, U. Influence of Defects on the Electronic Structure of Zinc Oxide Surfaces. *Phys. Rev. B* **1980**, *22* (12), 6447–6462. https://doi.org/10.1103/PhysRevB.22.6447.
(38) Morishige, K. Thermal Desorption Study of Surface Hydroxyls on ZnO. *J. Chem. Soc. Faraday Trans. 1* **1980**, *76*, 728.
(39) Zhang, S. B.; Wei, S.-H.; Zunger, A. Intrinsic *n* -Type versus *p* -Type Doping Asymmetry and the Defect Physics of ZnO. *Phys. Rev. B* **2001**, *63* (7), 075205. https://doi.org/10.1103/PhysRevB.63.075205.
(40) Bourke, J. D.; Chantler, C. T. Measurements of Electron Inelastic Mean Free Paths in Materials. *Phys. Rev. Lett.* **2010**, 4.
(41) Huang, R.; Ye, S.; Sun, K.; Kiang, K. S.; de Groot, C. H. Fermi Level Tuning of ZnO Films Through Supercycled Atomic Layer Deposition. *Nanoscale Res. Lett.* **2017**, *12* (1), 541. https://doi.org/10.1186/s11671-017-2308-1.
(42) Swallow, J. E. N.; Varley, J. B.; Jones, L. A. H.; Gibbon, J. T.; Piper, L. F. J.; Dhanak, V. R.; Veal, T. D. Transition from Electron Accumulation to Depletion at β-Ga $_2$ O $_3$ Surfaces: The Role of Hydrogen and the Charge Neutrality Level. *APL Mater.* **2019**, *7* (2), 022528. https://doi.org/10.1063/1.5054091.
(43) Lichterman, M. F.; Hu, S.; Richter, M. H.; Crumlin, E. J.; Axnanda, S.; Favaro, M.; Drisdell, W.; Hussain, Z.; Mayer, T.; Brunschwig, B. S.; Lewis, N. S.; Liu, Z.; Lewerenz, H.-J. Direct Observation of the Energetics at a Semiconductor/Liquid Junction by Operando X-Ray Photoelectron Spectroscopy. *Energy Environ. Sci.* **2015**, *8* (8), 2409–2416. https://doi.org/10.1039/C5EE01014D.
(44) Favaro, M.; Jeong, B.; Ross, P. N.; Yano, J.; Hussain, Z.; Liu, Z.; Crumlin, E. J. Unravelling the Electrochemical Double Layer by Direct Probing of the Solid/Liquid Interface. *Nat. Commun.* **2016**, *7* (1), 1–8. https://doi.org/10.1038/ncomms12695.
(45) Neppl, S.; Mahl, J.; Roth, F.; Mercurio, G.; Zeng, G.; Toma, F.; Huse, N.; Feulner, P.; Gessner, O. Nanoscale Confinement of Photo-Injected Electrons at the N3/ZnO Interface. *(submitted)* **2021**.
(46) Eger, D.; Many, A.; Goldstein, Y. Quantum Properties of Strong Accumulation Layers on ZnO Surfaces. *Surf. Sci.* **1976**, *58* (1), 18–24. https://doi.org/10.1016/0039-6028(76)90107-2.
(47) Bauer, C.; Boschloo, G.; Mukhtar, E.; Hagfeldt, A. Ultrafast Relaxation Dynamics of Charge Carriers Relaxation in ZnO Nanocrystalline Thin Films. *Chem. Phys. Lett.* **2004**, *387* (1–3), 176–181. https://doi.org/10.1016/j.cplett.2004.01.106.

For table of contents only: